X-Band Quasi-Elliptic Non-Reciprocal Bandpass Filters (NBPFs)

Andrea Ashley, *Graduate Student Member, IEEE*, and Dimitra Psychogiou, *Senior Member, IEEE*

***Abstract*— This article reports on the design and practical development of RF co-designed MMIC components that exhibit the function of a bandpass filter and an RF isolator. They are based on cascaded non-reciprocal frequency-selective stages (NFSs), one-pole/two-transmission zero (TZ) multi-resonant stages, and impedance inverters. The combination of these components results in a two-port network that exhibits a non-reciprocal quasi-elliptic bandpass filter (NBPF) response in the forward direction and full RF signal cancellation in the reverse one. The operating principles of the NBPF are presented through various circuit-based design examples of low- and high-order configurations. For proof-of-concept demonstration purposes, NBPF prototypes were designed on an MMIC GaAs process and were experimentally validated at *X*-band. They include a two-pole/two-TZ NBPF and a three-pole/four-TZ NBPF.**

***Index Terms*— Bandpass filter (BPF), integrated circuit, isolator, miniaturization, MMIC filter, non-reciprocal filter, RF co-design.**

I. Introduction

NON-RECIPROCAL microwave components such as isolators and circulators are important elements of a wide range of communication, radar, and instrumentation systems. They are used to protect high-power RF sources from unwanted reflections (e.g., in RF power-handling test sets) [1] or to separate the transmitted and received RF signals in applications where the same frequency is used for the transmit and receive operation (e.g., in full-duplex transceivers) [2]. Despite their importance in emerging RF systems (e.g., in 5G front-ends), the difficulty to integrate ferrite-based circulators/isolators with IC-based platforms has hindered their practical development [3]–[6]. Similar trends are observed with other RF front-end components such as the transmit and receive bandpass filters (BPFs) [7]–[11] that are either made from large off-chip low-loss elements or suffer from high in-band insertion loss (IL) when integrated in IC platforms [12], [13].

To overcome the RF front-end size constraints imposed by the off-chip components, miniaturization techniques are being explored at the component and at the integration level. These include miniaturization through capacitive loading [14]–[18], through integration in high-permittivity substrates [19]–[22], or using lumped-element (LE) configurations [5], [23]–[26]. Transistor-based isolators [27]–[31] exploiting the inherent unilateral behavior of transistors have also been explored. They include: cascaded low noise amplifiers and attenuators [27], transistor-based stages in common base or common collector configurations [28], and the combination of couplers with non-reciprocal components [30]. These topologies exhibit small size when compared to conventional ferrite-based isolators; however, they tend to provide moderate levels of isolation (20–37 dB) and moderate loss (1.5–2.5) despite using gain producing elements (i.e., transistors). Furthermore, they are limited to frequencies lower than 6 GHz.

In yet another approach, RF front-end miniaturization is achieved through the co-design of BPFs with other RF front-end components such as power dividers [32] and amplifiers [33], [34]. More recently, RF co-designed components that simultaneously exhibit the function of an isolator and a BPF have been developed. In this manner, either the isolator or the BPF can be removed from the RF front-end chain, allowing to reduce its size and loss as shown in Fig. 1. Notable demonstrations in this area include non-reciprocal bandpass filters (NBPFs) using spatio-temporal modulated (STM) resonators [35]–[41] and transistor-based resonators [42]. STM-based NBPFs achieve non-reciprocity by modulating the frequency of their resonators through varactors and MEMS tuners [35]–[38], [40], [41]. However, these configurations exhibit high IL (3.7–5.5 dB in [35]–[37] and [39]), spurious modes close to the passband [36], and are limited to low frequencies of operation <1 GHz. The NBPFs in [42] are based on non-reciprocal resonators shaped by transistors and microstrip transmission lines. Despite being validated in *S*-band, their size is fairly large due to being materialized by a hybrid PCB integration scheme.

Taking into consideration the aforementioned limitations, this article discusses the design and practical development of a new class of fully-integrated NBPFs that aim to miniaturize the RF front-end size. This is achieved by: 1) combining the functions of two RF components within the volume of a single

Manuscript received September 17, 2020; revised December 17, 2020 and January 13, 2021; accepted March 12, 2021. Date of publication May 27, 2021; date of current version July 1, 2021. This work was supported in part by the National Defense Science and Engineering Graduate (NDSEG) Fellowship and in part by the National Science Foundation (NSF) under Grant ECCS-1941315. *(Corresponding author: Andrea Ashley.)*

Andrea Ashley is with the Department of Electrical, Computer, and Energy Engineering, University of Colorado Boulder, Boulder, CO 80309 USA (e-mail: andrea.ashley@colorado.edu).

Dimitra Psychogiou was with the Department of Electrical, Computer, and Energy Engineering, University of Colorado Boulder, Boulder, CO 80309 USA. She is now with the Department of Electrical and Electronic Engineering, University College Cork, Cork, T12 K8AF Ireland, and also with the Tyndall National Institute, Cork, T12 R5CP Ireland (e-mail: dpsychogiou@ucc.ie).

Color versions of one or more figures in this article are available at https://doi.org/10.1109/TMTT.2021.3081021.

Digital Object Identifier 10.1109/TMTT.2021.3081021

0018-9480 © 2021 IEEE. Personal use is permitted, but republication/redistribution requires IEEE permission.
See https://www.ieee.org/publications/rights/index.html for more information.

Authorized licensed use limited to: UNIVERSITY OF COLORADO. Downloaded on December 11,2021 at 20:21:34 UTC from IEEE Xplore. Restrictions apply.

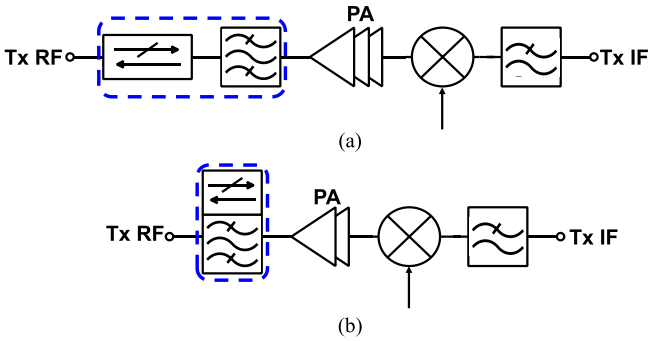

Fig. 1. High-power RF-front-end transmitter chain. (a) Conventional approach in which a BPF and an RF isolator are added after the power amplifier (PA) to cancel spurs and reflections. (b) Proposed approach leading to improved size and performance RF front-end through the devised RF co-designed NBPF that combines the function of a BPF and an RF isolator into a single device (boxed in blue). The NBPF can be designed with enhanced power transmission response, thus relaxing the gain requirements of the PA stage.

RF device; 2) MMIC integration; and 3) by allowing to relax the gain requirements in the PA stage through enhanced power transmission. The proposed NBPF concept is developed on a GaAs MMIC platform and is demonstrated experimentally at X-band. It is based on the cascade of non-reciprocal frequency-selective (NFS) gain stages and multiple multi-resonant stages through impedance inverters. The proposed GaAs MMIC NBPF enables quasi-elliptic bandpass-type transfer functions in the forward direction and high isolation in the reverse one. The content of this article is organized as follows. Section II, discusses the operating principles of the NFS and its use in the design of NBPFs with quasi-elliptic enhanced power transmission response in the forward direction and high isolation in the reverse one. In Section III, the practical implementation of the NBPF concept in an MMIC GaAs process is discussed through the design and experimental testing of two prototypes at X-band. They include: a two-resonator/two-transmission zero (TZ) NBPF and a three-resonator/four-TZ NBPF. Lastly, the main contributions of this article are summarized in Section IV.

II. Design Methodology

This section discusses the RF design and operating principles of the quasi-elliptic NBPF concept. It starts by introducing the basic functions of the proposed two-port NFS and continues with its use in high-order NBPFs with quasi-elliptic enhanced power transmission in the forward direction and high in-band isolation in the reverse one.

A. Non-Reciprocal Frequency-Selective Stage (NFS)

The details of the two-port NFS are illustrated in Fig. 2 in terms of its ideal block diagram and circuit-simulated power transmission ($|S_{21}|$), isolation ($|S_{12}|$) and reflection responses ($|S_{11}|$, $|S_{22}|$). It comprises a directional coupler (shaped by two pairs of transmission lines (TLs) with characteristic impedances Z_A and Z_B at the design frequency f_{cen}) and a non-reciprocal RF signal path that includes a non-reciprocal element (NRE) and additional phase control elements (i.e., TLs with characteristic impedance Z_C and electrical length θ_C). For the case of an ideal NRE, all TLs are 90°-long at f_{cen}.

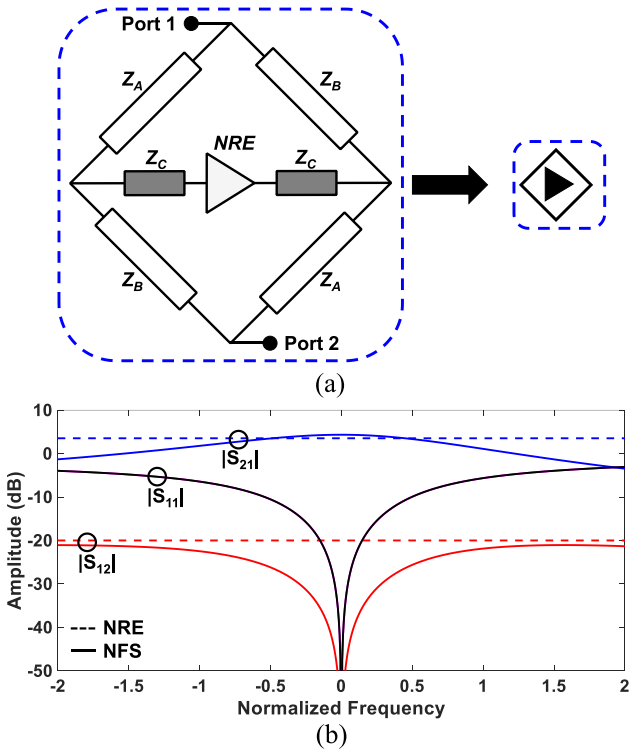

Fig. 2. NFS with enhanced power transmission response in the forward direction $|S_{21}|$ and complete RF signal cancellation in the reverse one $|S_{12}|$. (a) Block diagram and symbol, white and grey rectangles represent 90°-long transmission lines at f_{cen}, white triangle: NRE with or without gain. (b) Ideal power transmission ($|S_{21}|$), isolation ($|S_{12}|$), and reflection ($|S_{11}|$, $|S_{22}|$) responses of the NFS (solid lines) and its corresponding NRE (dashed lines). The element values for this example are: $Z_A = 11.9\ \Omega$, $Z_B = 71.1\ \Omega$, $Z_C = 12.1\ \Omega$, NRE S-parameters: $S_{11} = 0$, $S_{12} = 0.17$, $S_{21} = 1.5$, and $S_{22} = 0$.

The non-reciprocal RF signal path is connected between the through- and coupled-ports of the coupler allowing for higher levels of gain and theoretically-infinite isolation to be obtained at f_{cen} when compared to the single NRE, as shown in Fig. 2(b). The resulting two-port network leads to an NFS with a single-pole bandpass-type transfer function in the forward direction ($|S_{21}|$) and a bandstop-type single-TZ transfer function in the reverse direction ($|S_{12}|$).

To better illustrate the operating principles of the NFS, various design examples are shown in Fig. 3 for the case of an ideal NRE with finite gain and isolation characteristics ($S_{11} = 0$, $S_{12} = 0.17$, $S_{21} = 1.5$, and $S_{22} = 0$). In particular, when Z_A, Z_B, and Z_C are defined by (1) (k is the coupling factor of a conventional coupler and Z_0 is the reference impedance [43]), it can be seen that k primarily affects the isolation levels, as shown in Fig. 3(a), and Z_0 affects the BW of the NFS, as demonstrated in Fig. 3(b). It should be noted that the optimum k value (i.e., for maximum isolation at f_{cen}) depends on the isolation levels of the NRE

$$Z_A = Z_0\sqrt{1-k};\quad Z_B = Z_0\sqrt{\frac{1-k}{k}};\ Z_C = Z_0. \tag{1}$$

B. Non-Reciprocal Bandpass Filters (NBPFs)

To increase the order of the two-port network and facilitate NBPFs with highly-selective power transmission response

Authorized licensed use limited to: UNIVERSITY OF COLORADO. Downloaded on December 11,2021 at 20:21:34 UTC from IEEE Xplore. Restrictions apply.

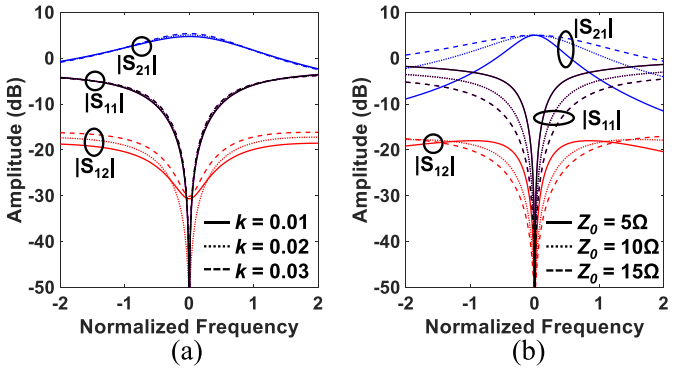

Fig. 3. RF power transmission ($|S_{21}|$), isolation ($|S_{12}|$), and reflection ($|S_{11}|$) response of the NFS as a function of (a) k when $Z_0 = 12.1\ \Omega$ and (b) Z_0 when $k = 0.028$. The NRE S-parameters are: $S_{11} = 0$, $S_{12} = 0.17$, $S_{21} = 1.5$, and $S_{22} = 0$.

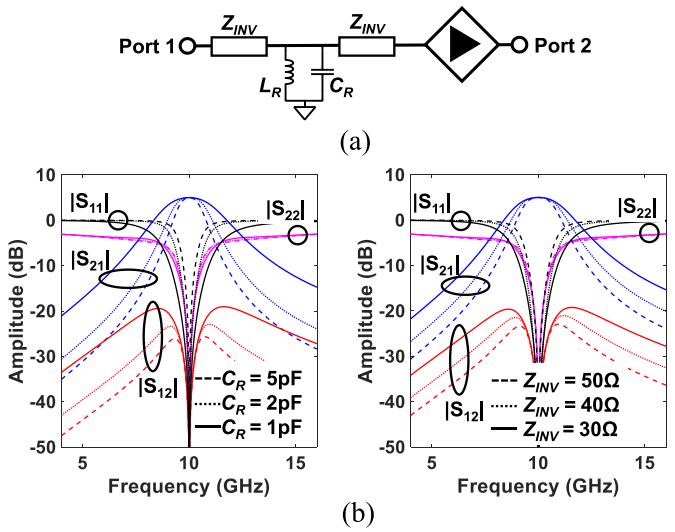

Fig. 4. (a) Block diagram of a two-resonator NBPF that comprises one NFS and one passive resonator. (b) Ideal linear circuit-simulated power transmission ($|S_{21}|$), isolation ($|S_{12}|$), and reflection ($|S_{11}|$, $|S_{22}|$) responses for varying BW. BW control when (C_R) is altered while L_R is selected to resonate with C_R (left) and BW control when Z_{INV} is altered (right). In all examples, the NRE S-parameters are as follows: $S_{11} = 0$, $S_{12} = 0.17$, $S_{21} = 1.5$, and $S_{22} = 0$.

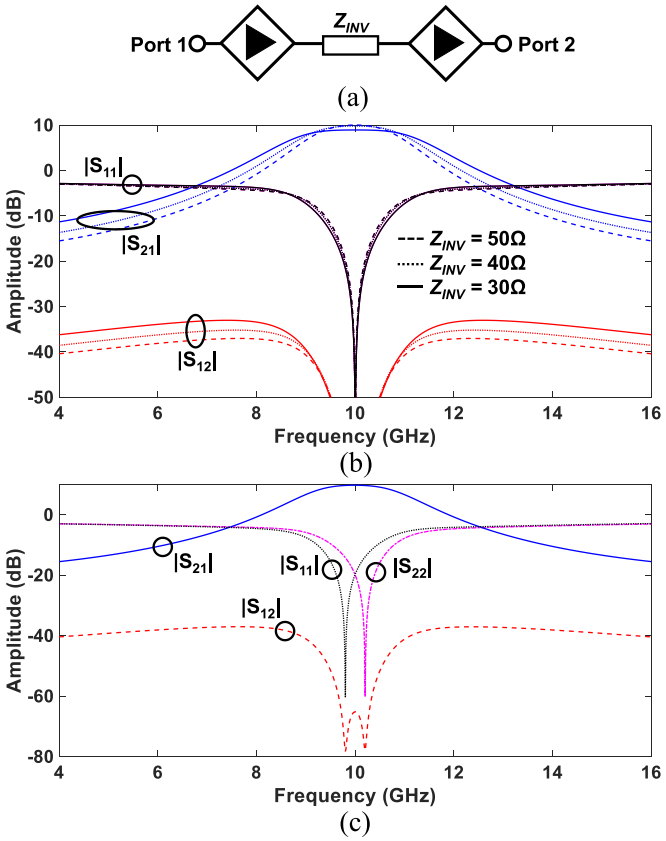

Fig. 5. (a) Block diagram of a two-resonator NBPF based on two series cascaded NFSs through an impedance inverter Z_{INV}. (b) Ideal linear circuit simulated power transmission ($|S_{21}|$), isolation ($|S_{12}|$), and reflection ($|S_{11}|$) response for varying BW. BW control when the when Z_{INV} is altered. (c) Simulated S-parameters for two dissimilar NFSs designed for maximum isolation at 9.8 and 10.2 GHz. The NRE S-parameters are as follows: $S_{11} = 0$, $S_{12} = 0.17$, $S_{21} = 1.5$, and $S_{22} = 0$.

in the forward direction and high isolation in the reverse one, architectures of cascaded NFSs and alternative types of reciprocal resonant elements can be considered, as shown in Figs. 4–9. In particular, Fig. 4 demonstrates a NBPF that comprises one passive resonator (C_R, L_R) and one NFS allowing to increase selectivity while maintaining the same levels of gain and isolation as in the NFS in Fig. 2. The passband BW in the forward direction can be controlled by either altering the capacitance C_R of the passive resonator (L_R needs to resonate with C_R) or by altering the impedance of Z_{INV} (inverter implemented with a 90°-long TL at f_{cen}) as shown in Fig. 4(b).

In Fig. 5(a) and (b), an NBPF configuration shaped by two identical NFSs is considered. In this case, the passband selectivity is the same as the one obtained in the example case in Fig. 4; however, the gain and isolation are essentially doubled due to the use of an additional NFS. In this architecture, the passband BW can be controlled by altering the impedance of Z_{INV} as shown in the examples in Fig. 5(b). Furthermore, when two dissimilar NFSs are considered, the TZs in the reverse direction can be split as shown in the example in Fig. 5(c).

In yet another configuration, the selectivity in the forward direction can be increased by cascading the NFS with a reciprocal multi-resonant stage as shown in Fig. 6. The multi-resonant stage is made from two open-ended stubs that result in one pole and two TZs. The stubs are 90°-long at the frequency of their corresponding TZ (f_{TZ1}, f_{TZ2}) and create a pole at the average frequency of f_{TZ1}, f_{TZ2} that is equal to f_{cen}. In this manner, a two-pole/two-TZ quasi-elliptic bandpass-type power transmission response can be obtained in the forward direction. Furthermore, as also shown in Fig. 6(b), the BW of frequencies at which the reverse transmission $|S_{12}|$ is lower than 20 dB is wider than in the NFS case in Fig. 2 due to the presence of three distinct TZs. Examples showing BW control in the forward direction are also included in Fig. 6(c) and (d). They are obtained using the impedance element values in Table I. As shown, the passband BW can be controlled by altering Z_{INV} and Z_{INV1} [Fig. 6(c)] or the location of the TZs [Fig. 6(d)]. While all of

Authorized licensed use limited to: UNIVERSITY OF COLORADO. Downloaded on December 11,2021 at 20:21:34 UTC from IEEE Xplore. Restrictions apply.

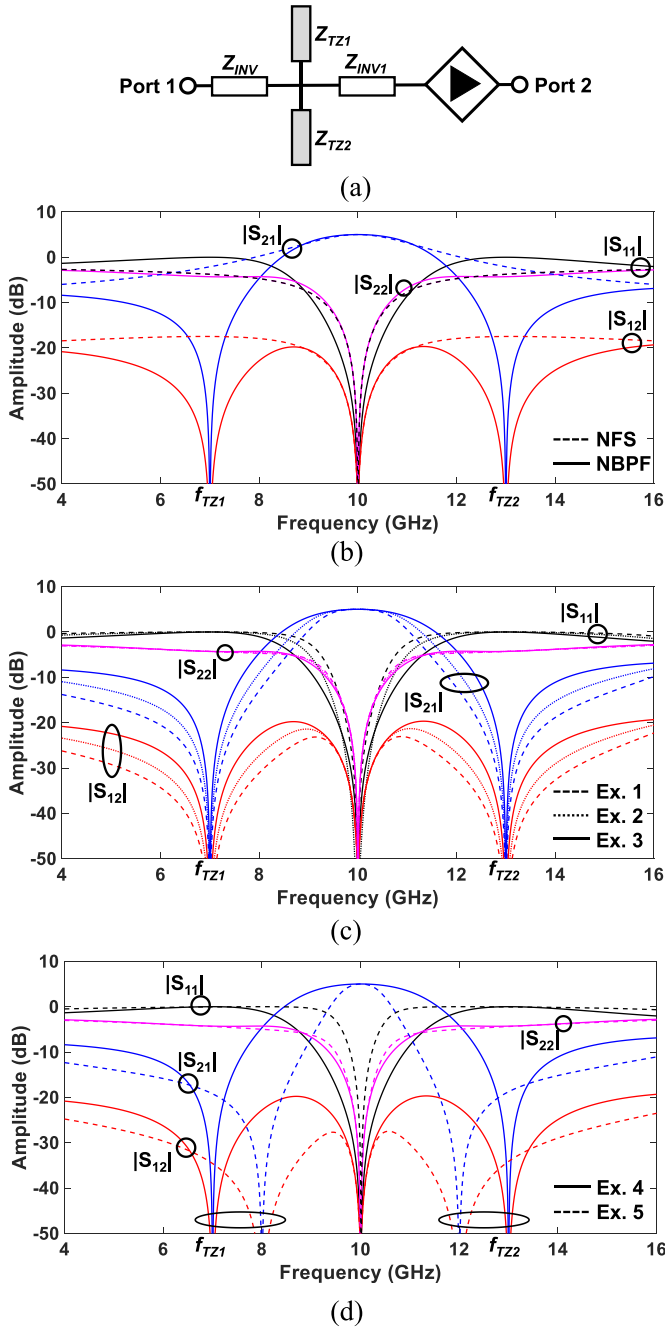

Fig. 6. (a) Block diagram of a two-resonator/two-TZ NBPF that comprises one NFS and one multi-resonant stage. (b) Comparison of the circuit-simulated power transmission ($|S_{21}|$), isolation ($|S_{12}|$), and reflection responses ($|S_{11}|$, $|S_{22}|$) of the NFS and the NBPF. (c) Ideal circuit-simulated response of the power transmission ($|S_{21}|$), isolation ($|S_{12}|$), and reflection ($|S_{11}|$, $|S_{22}|$) for varying BW by altering the impedance of the inverters. (d) Ideal circuit-simulated response of the power transmission ($|S_{21}|$), isolation ($|S_{12}|$), and reflection ($|S_{11}|$, $|S_{22}|$) for varying BW by altering the location of the TZs. The impedance element values for these examples are listed in Table I whereas the NRE S-parameters are as follows: $S_{11} = 0$, $S_{12} = 0.17$, $S_{21} = 1.5$, and $S_{22} = 0$.

the previous examples show a single reflection zero, in fact multiple reflection poles are present at the center frequency (two in this case). The reflection poles can be split by altering the impedance of the impedance inverter Z_{INV1} as shown in Fig. 7.

TABLE I
ELEMENT VALUES OF THE EXAMPLE RESPONSES IN FIG. 6

Example	1	2	3	4	5
Z_{INV}	30	40	50	50	50
Z_{INV1}	30	40	50	50	50
Z_{TZ1}	30	30	30	30	34
Z_{TZ2}	63	63	63	63	53

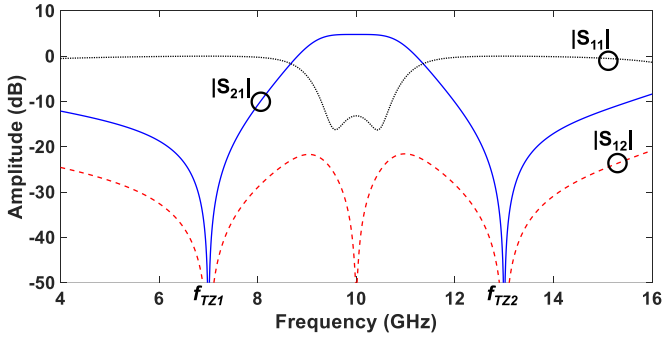

Fig. 7. S-parameters for the NBPF in Fig. 6(a) with separated reflection poles in the passband. The impedances for the inverters and multi-resonant cell are as follows: $Z_{INV} = 50\ \Omega$, $Z_{INV1} = 40\ \Omega$, $Z_{TZ1} = 30\ \Omega$, and $Z_{TZ2} = 63\ \Omega$.

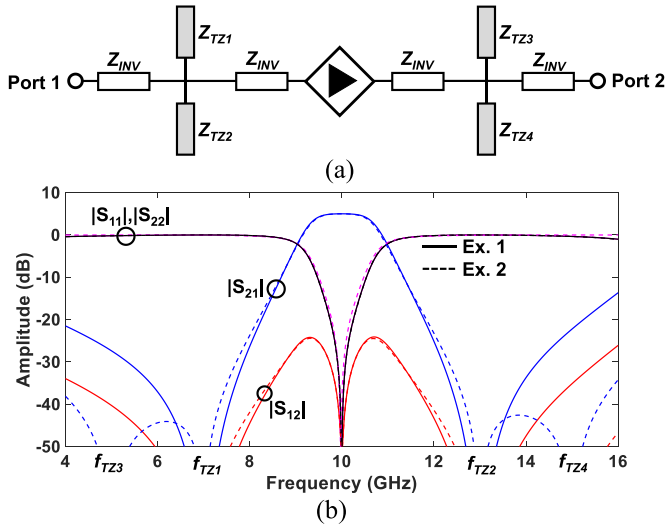

Fig. 8. (a) Block diagram for a three-resonator/four-TZ NBPF based on one NFS and two multi-resonant stages. (b) Comparison of the circuit-simulated power transmission ($|S_{21}|$), isolation ($|S_{12}|$), and reflection responses ($|S_{11}|$, $|S_{22}|$) for identical (Ex. 1) and non-identical multi-resonant stages (Ex. 2).

To further increase the passband selectivity and the out-of-band rejection in the forward direction, an additional multi-resonant stage can be added at the output of the NBPF to create a three-resonator/four-TZ configuration as shown in Fig. 8(a). In this manner, a three-pole/four-TZ power transmission response can be obtained in the forward direction and a five-TZ response in the reverse one. The multi-resonant stages can be designed to create TZs at identical or at different frequencies with the purpose of increasing the out-of-band

Authorized licensed use limited to: UNIVERSITY OF COLORADO. Downloaded on December 11,2021 at 20:21:34 UTC from IEEE Xplore. Restrictions apply.

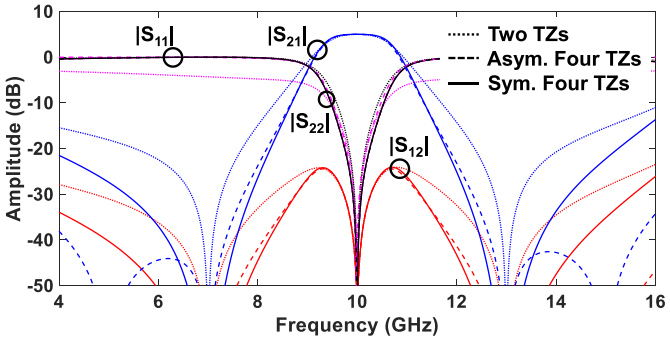

Fig. 9. Comparison of the S-parameters of the NBPFs in Fig. 6 (dotted lines) and Fig. 8 (solid and dashed lines).

TABLE II
ELEMENT VALUES OF THE EXAMPLE RESPONSES IN FIG. 8

Example	1	2
Z_{INV}	50	50
Z_{TZ1}	30	30
Z_{TZ2}	63	63
Z_{TZ3}	30	8
Z_{TZ4}	63	4000
f_{TZ1}	7 GHz	7 GHz
f_{TZ2}	13 GHz	13 GHz
f_{TZ3}	7 GHz	5 GHz
f_{TZ4}	13 GHz	15 GHz

isolation BW in the forward direction as shown in the example cases in Fig. 8(b). The impedance inverter values for these examples are provided in Table II. Fig. 9 demonstrates a comparison of the S-parameter response of the two-resonator/two-TZ and the three-resonator/four-TZ NBPFs. As it can be seen, by adding the multi-resonant stage at the output, the frequency selectivity and the out-of-band isolation in the forward direction are increased, demonstrating the selectivity-enhancement advantages of the proposed approach.

Although a finite number of NBPF examples are discussed in this section, the proposed approach can be readily scaled to the realization of transfer functions with even higher order and gain or wider out-of-band rejection BW in the forward direction or higher isolation in the reverse direction by appropriately selecting the number of the NFSs, passive resonators, and multi-resonant stages.

C. NRE Practical Realization Aspects

While an ideal NRE has been considered in all previous example cases, realistic NRE implementations may exhibit a phase shift (as shown in the actual MMIC NRE design in Section III) which needs to be considered in the NFS design. This is illustrated in Fig. 10, in which the S-parameter response of an NFS comprising an NRE with and without phase shift are compared. As shown, a finite phase shift in the NRE results in finite isolation at f_{cen}. In order for the maximum gain and maximum isolation to occur at the same operating frequency, the electrical length of Z_A (θ_A), Z_B (θ_B),and Z_C(θ_C), need to be adjusted. In this example, a non-ideal NRE with $+45°$ in the forward direction and $-29°$ in the reverse direction is

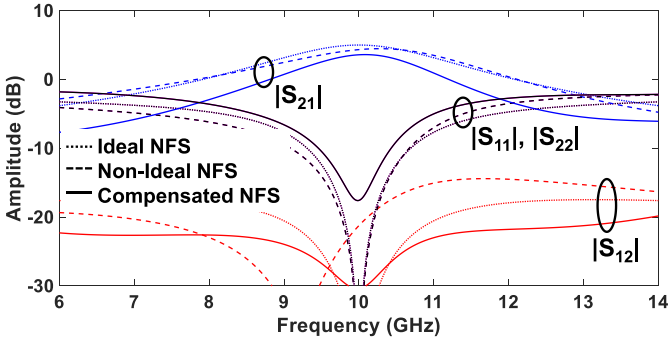

Fig. 10. Comparison of the S-parameter responses of an NFS with an ideal NRE (dotted trace), an NFS with a non-ideal NRE (dashed trace), and an NFS with a non-ideal NRE with the phase of Z_A, Z_B, and Z_C altered to compensate for the phase of the NRE (solid trace). The S-parameters for the non-ideal NRE are as follows: $S_{11} = 0$, $S_{12} = 0.15 - j0.08$, $S_{21} = 1.1 + j1.1$, and $S_{22} = 0$.

considered. As it can be seen, the location of the maximum isolation point is shifted lower in frequency. To compensate for this frequency shift, the electrical lengths of the TLs were selected as follows: $\theta_A = 100°$, $\theta_B = 100°$, and $\theta_C = 82°$. This adjustment realigns the maximum gain and isolation frequencies to occur at f_{cen}, however, the BW, gain, and match levels slightly differ than the response of the ideal NRE.

III. EXPERIMENTAL VALIDATION

To evaluate the validity of the NBPF concept, two prototypes were designed, manufactured, and measured at *X*-band using the WIN Semiconductor PIH1-10 MMIC GaAs process, circuit, and full-wave electromagnetic (EM) analysis in AWR, Cadence. They include: 1) a two-pole/two-TZ NBPF with $f_{\text{cen}} = 9.0$ GHz and FBW $= 7.5\%$ based on the block diagram in Fig. 6 and 2) a three-pole/four-TZ NBPF with $f_{\text{cen}} = 9.0$ GHz and FBW $= 8.1\%$ based on the block diagram in Fig. 8.

A. MMIC NRE/NFS Design

The NRE was designed in the PIH1-10 MMIC GaAs process of WIN Semiconductors; which consists of three metal layers (metal 1, metal 2, and ground), as shown in Fig. 11. It was designed with the purpose of providing gain (two-finger pHEMT transistor biased at $V_{\text{DD}} = 2.5$ V, and $V_G = 0.65$ V) at the operating frequency while maintaining stability by adding the gate and drain matching networks in Fig. 11(b). The S-parameters of the NRE are provided in Fig. 11(c) in terms of magnitude and phase. As shown, it exhibits a phase offset in both the forward and reverse directions which is compensated in the NFS by altering the phase of TLs (θ_A, θ_B, and θ_C) as discussed in Section II-C. The TL characteristics were selected as follows: $Z_A = 23.5\ \Omega$, $\theta_A = 80°$, $Z_B = 140\ \Omega$, $\theta_B = 80°$, and $Z_C = 27\ \Omega$, $\theta_C = 72°$ ($k = 0.028$, $Z_0 = 23.8\ \Omega$) to create the overall NFS response in Fig. 12. As it can be seen, the depth of the isolation zero is not infinite. This is due to the manufacturing limitations of the process. In particular, to achieve a high isolation at the center frequency, k would need to be 0.0072 and $Z_0 = 23.8\ \Omega$. Using (1), this would result in the following

Authorized licensed use limited to: UNIVERSITY OF COLORADO. Downloaded on December 11,2021 at 20:21:34 UTC from IEEE Xplore. Restrictions apply.

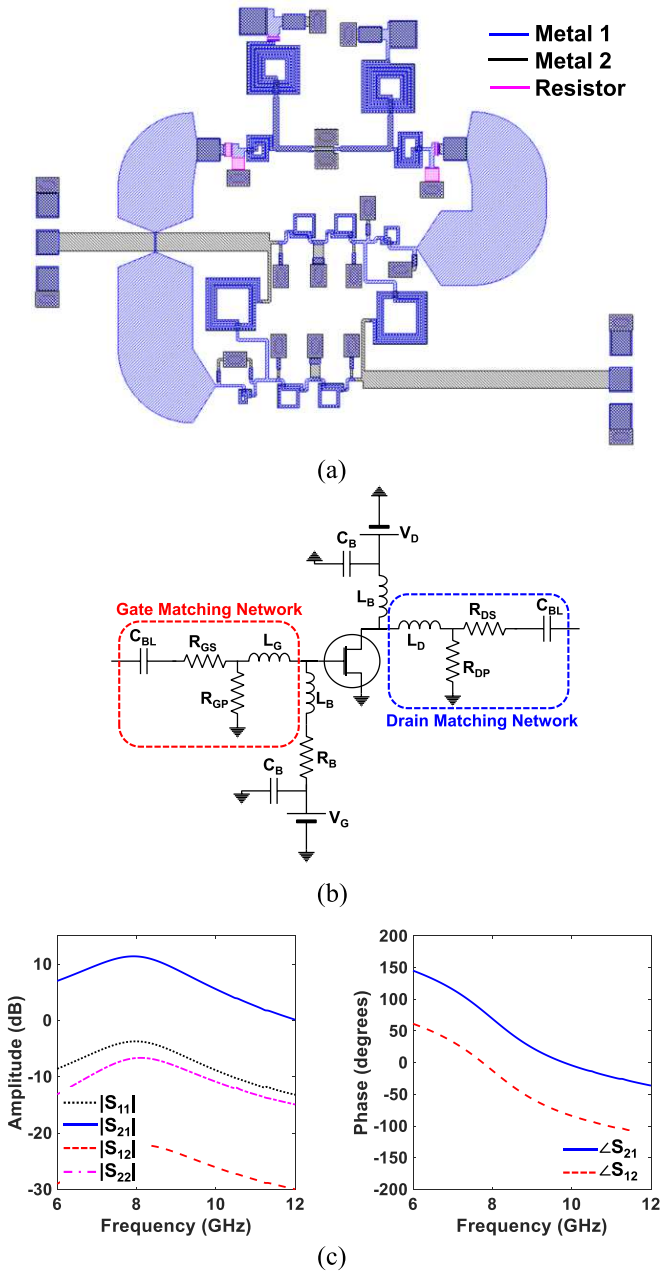

Fig. 11. (a) Layout of the NFS. (b) Circuit schematic of the NRE. Its element values are as follows: $C_{\mathrm{BL}} = 3.2$ pF, $L_B = 13$ nH, $C_B = 2.1$ pF, $R_B = 10.1\ \Omega$, $R_{\mathrm{GS}} = 21.6\ \Omega$, $R_{\mathrm{GP}} = 45.1\ \Omega$, $L_G = 0.48$ nH, $L_D = 0.79$ nH, $R_{\mathrm{DS}} = 10.1\ \Omega$, $R_{\mathrm{DP}} = 45.5\ \Omega$, $V_G = 0.65$ V, and $V_B = 2.5$ V. (c) S-parameters of the NRE in (b) in terms of magnitude (left) and phase (right).

impedances: $Z_A = 23.7\ \Omega$, $Z_B = 280\ \Omega$, and $Z_C = 23.8\ \Omega$. In this case, Z_B is too large to manufacture, therefore the k had to be altered, resulting in finite isolation at the center frequency when compared to the ideal scenarios in Section II. Furthermore, since Z_C was implemented using a microstrip TL, its characteristic impedance was also limited by the manufacturing process.

B. Two-Pole/Two-TZ NBPF

To validate the quasi-elliptic NBPF concept in Fig. 6, a two-resonator/two-TZ NBPF was designed for $f_{\mathrm{cen}} = 8.8$ GHz, FBW $= 11.3\%$ and two TZs at 7.75 and 9.9 GHz. The

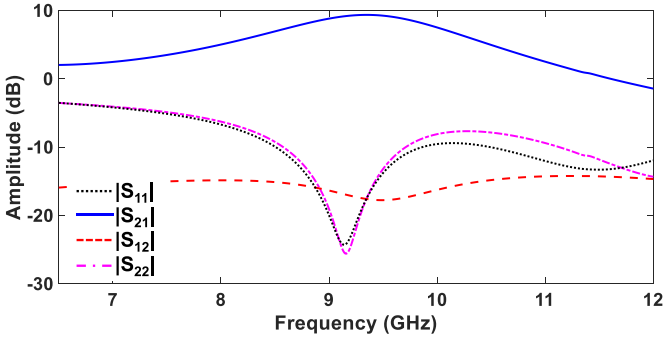

Fig. 12. Circuit-simulated S-parameters for the NFS in Fig. 11(a).

photograph of the GaAs MMIC manufactured prototype is shown in Fig. 13(a) alongside its different counterparts. The NBPF was designed using the NFS in Fig. 11, where for size compactness, Z_A and Z_B were implemented on metal 1 through their low-pass LE π-type circuit equivalent. The Z_C TLs were materialized on metal 1 through a hybrid implementation approach in which a 30°-long part of the TL was implemented by a microstrip TL and the rest by a LE artificial TL. Since the RF input and output ports were placed on the edge of the chip, they were implemented on metal 2 layer to prevent overlap with the rest of the components on metal 1. The multi-resonant stage (circled in green) was made by two capacitively-loaded microstrip TLs and the inverters Z_{INV}, which were approximately equivalent to 15 Ω (circled in red). They were implemented by their LE TL equivalents for size compactness. In particular, the external coupling was materialized by its high-pass first-order π-type LE circuit equivalent whereas the inter-resonator coupling was materialized by its low-pass first-order π-type circuit equivalent.

The RF measured performance of the two-resonator/two-TZ NBPF is depicted in Fig. 13(b) and (c) and is summarized as follows: $f_{\mathrm{cen}} = 9.0$ GHz, FBW $= 7.5\%$, maximum in-band gain ($|S_{21}|$) $= 4.2$ dB, and maximum in-band IS $= 31.3$ dB. The simulated S-parameters are also shown at the same figure. As it can be seen in Fig. 13(b), the EM-simulated and RF-measured response are in a fair agreement. The small differences that are observed in the passband FBW and gain (1.7-dB gain difference and 3.8% FBW difference) are attributed to process manufacturing variations that led to the TZs in the measured response to move closer to the passband, thus reducing the FBW and gain. As it can be seen in Fig. 13(c), if the capacitance of the stubs in the multi-resonant stage are altered so that the TZs in the EM simulation line up with the ones in the RF measurements, then a very good agreement can be obtained, thus validating the proposed NBPF concept.

C. Three-Pole/Four-TZ NRF

To further increase the out-of-band isolation, a three-resonator/four-TZ NBPF was designed, manufactured and measured using as a basis the block diagram in Fig. 8. The photograph of the manufactured prototype is shown in Fig. 14(a). In this design, the multi-resonant stages were

Authorized licensed use limited to: UNIVERSITY OF COLORADO. Downloaded on December 11,2021 at 20:21:34 UTC from IEEE Xplore. Restrictions apply.

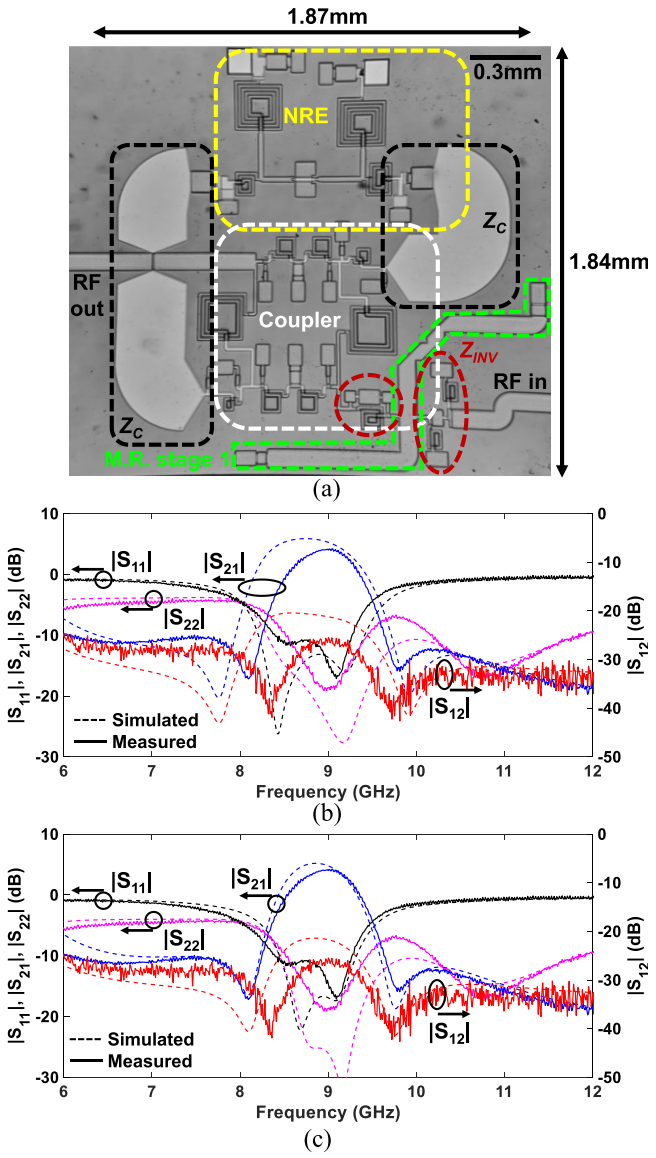

Fig. 13. (a) Photograph of the manufactured two-resonator/two-TZ prototype based on the block diagram in Fig. 6(a). The NRE is circled in yellow, the coupler is circled in white, Z_C is circled in black, the multi-resonant stage 1 is circled in green, and the inverters Z_{INV} are circled in red. (b) RF-measured and EM-simulated S-parameters for the two-resonator/two-TZ NBPF prototype in (a). (c) RF-measured and fitted EM-simulated S-parameters for the two-resonator/two-TZ NBPF prototype in (a).

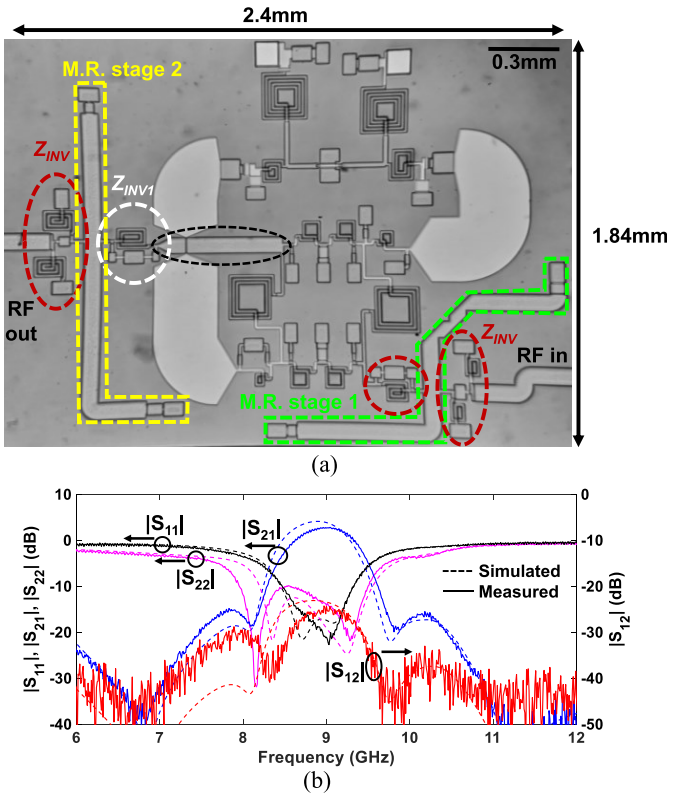

Fig. 14. (a) Photograph for the manufactured three-resonator/four-TZ prototype based on the block diagram in Fig. 8(a). The second multi-resonant stage is circled in yellow, Z_{INV} is circled in red, Z_{INV1} is circled in white, the line needed to prevent overlap between the NFS is circled in black, and the multi-resonant stage 1 is circled in green. (b) Measured and EM-simulated S-parameters for the three-resonator/four-TZ prototype in (a).

designed with capacitively-loaded TLs to have TZs at 6.9 and 11.2 GHz (circled in yellow) and 8.1 and 9.8 GHz (circled in green). Similar to the design in Fig. 13(a), the inverters were designed using their LE TL equivalents for size compactness; where Z_{INV} (circled in red) was equivalent to 15 Ω. It is worth noting that Z_{INV1} (which is the coupling between the NFS and multi-resonant stage 2), differed from Z_{INV} order to compensate for the additional line length (circled in black) that was required to prevent overlap between the inverter and NFS, as shown in Fig. 14(a). In particular, Z_{INV1}(circled in white) was approximately equivalent to 40 Ω since it could not directly be connected to the NFS. The overall NBPF was designed to operate at 9.0 GHz with FBW of 8.0%. The RF performance is shown in Fig. 14(b) and is summarized as follows: $f_{cen} = 9.0$ GHz, FBW = 8.1%, maximum gain ($|S_{21}|$) = 2.8 dB, and maximum IS = 28.8 dB. The fitted EM-simulated response is also provided in the same figure which as shown agrees well with the RF measured one.

D. Comparison With State-of-the-Art (SOA)

A comparison of the proposed MMIC NBPFs with other SOA NBPFs and IC-based isolators is provided Table III. As it can be seen, the proposed concept is the only GaAs MMIC component that facilitates the realization of two RF functions (i.e., a quasi-elliptic BPF and an RF isolator) within the volume of a single front-end element. Furthermore, it exhibits higher operational frequency and higher gain than SOA NBPFs and isolators and it is the only transistor-based component that allows the realization of TZs in its out-of-band response. In addition, when compared to the NBPFs [35], [36], [39]–[42], the proposed topology results in the smallest physical footprint. As shown in Table III, the IC-based components in [27]–[30] only exhibit the function of an RF isolator and show loss in their passband. While the isolators in [27]–[30] provide smaller size than the proposed concept, they would need additional BPFs to be cascaded in series to create the same filtering response. This addition would in turn increase

Authorized licensed use limited to: UNIVERSITY OF COLORADO. Downloaded on December 11,2021 at 20:21:34 UTC from IEEE Xplore. Restrictions apply.

TABLE III
COMPARISON OF THE PROPOSED NBPFS WITH SOA ISOLATORS AND NBPFS

Ref.	Component & approach	f_{cen} (GHz)	FBW (%)	$\|S_{21}\|$ (dB)	IS (dB)	Filtering Capabilities	Res./TZs	Size (mm x mm)	Size (λ x λ)
[27]	Transistor-based isolator, MMIC	1.4	14.3	-2.5	31	No	0/0	0.93 x 0.687	0.004 x 0.003
[28]	Transistor-based isolator, SiGe	5.5	N/A	-2	35	No	0/0	0.64 x 0.43	0.012 x 0.008
[30]	Transistor-based isolator, CMOS	24	N/A	-1.8	36.7	No	0/0	0.66 x 0.435	0.053 x 0.035
[35]	STM NBPF, hybrid PCB	0.14	19.2	-3.7	52.8	Yes	3/0	N/A	N/A
[36]	STM NBPF, hybrid PCB	1	6.3	-5.5	6.2	Yes	2/0	20.7 x 18.3	0.069 x 0.061
[39]	STM NBPF, hybrid PCB	1.175	1.7	-4.5	28	Yes	3/0	N/A	N/A
[40]	STM NBPF, hybrid PCB	0.2	15	-1.5	20	Yes	3/0	N/A	N/A
[41]	STM NBPF, hybrid PCB	1	4.2	-3.9	23.2	Yes	3/2	15.02 x 25.28	0.05 x 0.084
[42]	Transistor-based NBPF, hybrid PCB	2.2	9.3	5.6	44	Yes	2/0	39.2 x 48	0.287 x 0.352
This work	Transistor-based NBPF, MMIC 2	9.0	7.5	4.2	31.3	Yes	2/2	1.87 x 1.84	0.056 x 0.055
	Transistor-based NBPF, MMIC 3	9.0	8.1	2.8	28.8	Yes	3/4	2.4 x 1.84	0.072 x 0.055

the overall size and IL of the RF front-end. The STM-based NBPFs in [35] and [36] and [39]–[41] are limited to frequencies up to 1.2 GHz, show high levels of loss (i.e., $|S_{21}| = -5.5$ dB in [36]) and require complex biasing methods (e.g., spatio-temporal modulation in [35]–[39]). The NBPF in [41] has TZs in the out-of-band response; however, it demonstrates high levels of IL (3.9 dB) and moderate IS (23.2 dB). While the co-designed NBPF in [42] exhibits higher IS and its gain is comparable to the proposed concept, it operates at a lower frequency and is based on a completely different implementation scheme. Furthermore, it exhibits significantly larger footprint due to its hybrid PCB integration.

IV. CONCLUSION

This article presented the operational principles and practical implementation aspects of a new class of MMIC RF components that exhibit the function of a BPF and an RF isolator. The proposed NBPFs are based on cascaded NFSs, multi-resonant stages and impedance inverters. The operational principles of the NBPF concept and its extension to high order transfer functions were presented through circuit-based analysis. For proof-of-concept validation purposes, two prototypes were designed and measured at *X*-band using the WIN Semiconductor GaAs process. They include: 1) two-resonator/two-TZ NBPF and 2) a three-resonator/four-TZ NRF. To the best of the authors' knowledge this is the first demonstration of a fully integrated NBPF with enhanced power transmission in the forward direction, high isolation in the reverse direction, and increased out-of-band isolation through the presence of TZs.

ACKNOWLEDGMENT

The authors would like to thank WIN Semiconductors Corporation for providing access to their PIH1-10 process and for manufacturing the MMIC components.

REFERENCES

[1] I. C. Reines and G. M. Rebeiz, "A robust high power-handling (> 10 W) RF MEMS switched capacitor," in *Proc. IEEE 24th Int. Conf. Micro Electro Mech. Syst.*, Cancun, Mexico, Jan. 2011, pp. 764–767.

[2] M. A. Islam and B. Smida, "A comprehensive self-interference model for single-antenna full-duplex communication systems," in *Proc. IEEE Int. Conf. Commun. (ICC)*, Shanghai, China, May 2019, pp. 1–7.

[3] X. Li, E. Li, and G. Guo, "Design of X-band H-plane waveguide Y-junction circulator," in *Proc. Int. Workshop Microw. Millim. Wave Circuits Syst. Technol.*, Chengdu, China, Apr. 2012, pp. 1–4.

[4] S. Yang, D. Vincent, J. R. Bray, and L. Roy, "Ferrite LTCC edge-guided circulator," in *Proc. 44th Eur. Microw. Conf.*, Rome, Italy, 2014, pp. 1540–1543.

[5] H. Dong, J. R. Smith, and J. L. Young, "A wide-band, high isolation UHF lumped-element ferrite circulator," *IEEE Microw. Wireless Compon. Lett.*, vol. 23, no. 6, pp. 294–296, Jun. 2013.

[6] W. Marynowski, "Integrated broadband edge-guided mode isolator with antiparallel biasing of the ferrite slabs," *IEEE Microw. Wireless Compon. Lett.*, vol. 28, no. 5, pp. 392–394, May 2018.

[7] R. Gómez-Garcia, J.-M. Muñoz-Ferreras, W. Feng, and D. Psychogiou, "Balanced symmetrical quasi-reflectionless single-and dual-band bandpass planar filters," *IEEE Microw. Wireless Compon. Lett.*, vol. 28, no. 9, pp. 798–800, Sep. 2018.

[8] J. Xu, "Compact quasi-elliptic response wideband bandpass filter with four transmission zeros," *IEEE Microw. Wireless Compon. Lett.*, vol. 25, no. 3, pp. 169–171, Mar. 2015.

[9] U.-H. Lok, Y.-C. Chiou, and J.-T. Kuo, "Quadruple-mode coupled-ring resonator bandpass filter with quasi-elliptic function passband," *IEEE Microw. Wireless Compon. Lett.*, vol. 18, no. 3, pp. 179–181, Mar. 2008.

[10] D. Psychogiou, R. Gómez-Garcia, and D. Peroulis, "Adaptive-transfer-function bandpass filters using reconfigurable evanescent-mode-cavity resonator cascades," in *IEEE MTT-S Int. Microw. Symp. Dig.*, San Francisco, CA, USA, May 2016, pp. 1–4.

[11] R. Loeches-Sánchez, D. Psychogiou, D. Peroulis, and R. Gómez-Garcia, "Sharp-rejection highpass and dual-band bandpass planar filters with multi-transmission-zero-generation transversal cell," in *Proc. IEEE Radio Wireless Symp. (RWS)*, San Diego, CA, USA, Jan. 2015, pp. 147–149.

[12] M. Lei and H. Wang, "Implementation of reduced-size dual-mode ring filters in LTCC and MMIC processes at millimeter wave frequencies," in *Proc. Eur. Microw. Conf.*, Manchester, U.K., 2006, pp. 537–540.

[13] E. P. Sinulingga, A. R. Nasution, and P. B. Kyabaggu, "Perturbation effect on a dual mode CPW multilayer MMIC bandpass filter," in *Proc. 3rd Int. Conf. Electr., Telecommun. Comput. Eng. (ELTICOM)*, Medan, Indonesia, Sep. 2019, pp. 66–69.

[14] A. Ashley, L. F. Marzall, Z. Popovic, and D. Psychogiou, "Frequency selective ferrite circulators with quasi-elliptic transmission response," in *Proc. 48th Eur. Microw. Conf. (EuMC)*, Madrid, Spain, Sep. 2018, pp. 211–214.

[15] C.-W. Tang, J.-W. Wu, C.-C. Hu, H.-C. Lin, and S.-S. Yeh, "The microstrip filter with multiple stacked capacitively-loaded coupled lines," in *Proc. Asia–Pacific Microw. Conf.*, Yokohama, Japan, Dec. 2006, pp. 1553–1556.

[16] M. Li, C. Chen, and W. Chen, "Miniaturized dual-band filter using dual-capacitively loaded SIW cavities," *IEEE Microw. Wireless Compon. Lett.*, vol. 27, no. 4, pp. 344–346, Apr. 2017.

[17] F. Aryanfar and K. Sarabandi, "Compact millimeter-wave filters using distributed capacitively loaded CPW resonators," *IEEE Trans. Microw. Theory Techn.*, vol. 54, no. 3, pp. 1161–1165, Mar. 2006.

Authorized licensed use limited to: UNIVERSITY OF COLORADO. Downloaded on December 11,2021 at 20:21:34 UTC from IEEE Xplore. Restrictions apply.

[18] A. Gorur, C. Karpuz, and M. Akpinar, "A reduced-size dual-mode bandpass filter with capacitively loaded open-loop arms," *IEEE Microw. Wireless Compon. Lett.*, vol. 13, no. 9, pp. 385–387, Sep. 2003.

[19] S. Hemour, S. Adhikari, A. Ghiotto, and K. Wu, "Low magnetic biased SIW-based isolator: Effect of the rising temperature on the performance of the isolator," in *Proc. WAMICON*, Tampa, FL, USA, Jun. 2014, pp. 1–3.

[20] Y. J. Cheng, Q. D. Huang, Y. R. Wang, and J. L.-W. Li, "Narrowband substrate integrated waveguide isolators," *IEEE Microw. Wireless Compon. Lett.*, vol. 24, no. 10, pp. 698–700, Oct. 2014.

[21] Q. Li *et al.*, "60 GHz substrate integrated waveguide resonance isolator," in *IEEE MTT-S Int. Microw. Symp. Dig.*, San Francisco, CA, USA, May 2016, pp. 1–3.

[22] S. Beguhn, X. Yang, and N. X. Sun, "Design of a magnetization gradient ferrite substrate integrated waveguide isolator to mitigate higher order mode effects," in *IEEE MTT-S Int. Microw. Symp. Dig.*, Seattle, WA, USA, Jun. 2013, pp. 1–3.

[23] T. Wada *et al.*, "A miniaturized broadband lumped element circulator for reconfigurable front-end system," in *IEEE MTT-S Int. Microw. Symp. Dig.*, Tampa, FL, USA, Jun. 2014, pp. 1–3.

[24] T. Hasegawa and T. Okada, "Low loss lumped element isolator using gyrator circuit with two asymmetrical electrodes," in *IEEE MTT-S Int. Microw. Symp. Dig.*, San Francisco, CA, USA, Jun. 2006, pp. 540–543.

[25] S. Takeda and H. Mikami, "Directly coupled lumped element isolator with three windings," in *Proc. Eur. Microw. Conf.*, Munich, Germany, 2007, pp. 278–281.

[26] T. Hasegawa, R. Nakajima, S. Ichiguchi, T. Wada, M. Koshino, and T. Okada, "Miniaturized lumped element isolator operating in weak magnetic field below ferromagnetic resonance," in *Proc. Asia–Pacific Microw. Conf.*, Melbourne, VIC, Canada, 2011, pp. 546–549.

[27] M. F. Cordoba-Erazo and T. M. Weller, "A 1.4 GHz MMIC active isolator for integrated wireless systems applications," in *Proc. WAMICON*, Tampa, FL, USA, Jun. 2014, pp. 1–3.

[28] J. Lee, J. D. Cressler, and A. J. Joseph, "A 5-6 GHz SiGe HBT monolithic active isolator for improving reverse isolation in wireless systems," *IEEE Microw. Wireless Compon. Lett.*, vol. 15, no. 4, pp. 220–222, Apr. 2005.

[29] D. G. Haigh, "Wideband active microwave isolators using GaAs MMIC technology," *IEE Proc.-Microw., Antennas Propag.*, vol. 143, no. 2, pp. 179–183, Apr. 1996.

[30] J.-F. Chang, J.-C. Kao, Y.-H. Lin, and H. Wang, "A 24-GHz fully integrated isolator with high isolation in standard RF 180-nm CMOS technology," in *IEEE MTT-S Int. Microw. Symp. Dig.*, Tampa, FL, USA, Jun. 2014, pp. 1–3.

[31] R. Pyndian and F. van den Bogaart, "Novel multioctave MMIC active isolator (1-20 GHz)," *Electron. Lett.*, vol. 25, no. 21, pp. 1420–1422, 12 Oct. 1989.

[32] R. Gomez-Garcia, J.-M. Munoz-Ferreras, and D. Psychogiou, "RF reflectionless filtering power dividers," *IEEE Trans. Circuits Syst. II, Exp. Briefs*, vol. 66, no. 6, pp. 933–937, Jun. 2019.

[33] K. Chen, J. Lee, W. J. Chappell, and D. Peroulis, "Co-design of highly efficient power amplifier and high-Q output bandpass filter," *IEEE Trans. Microw. Theory Techn.*, vol. 61, no. 11, pp. 3940–3950, Nov. 2013.

[34] Y. Gao *et al.*, "Substrate integrated waveguide filter–amplifier design using active coupling matrix technique," *IEEE Trans. Microw. Theory Techn.*, vol. 68, no. 5, pp. 1706–1716, May 2020.

[35] D. Simpson and D. Psychogiou, "Magnet-less non-reciprocal bandpass filters with tunable center frequency," in *Proc. 49th Eur. Microw. Conf. (EuMC)*, Paris, France, 2019, pp. 460–463.

[36] X. Wu, M. Nafe, A. A. Melcón, J. S. Gómez-Díaz, and X. Liu, "A non-reciprocal microstrip bandpass filter based on spatio-temporal modulation," in *IEEE MTT-S Int. Microw. Symp. Dig.*, Boston, MA, USA, Jun. 2019, pp. 9–12.

[37] X. Wu, M. Nafe, and X. Liu, "Non-reciprocal 2nd-order bandpass filter by using time-modulated microstrip quarter-wavelength resonators," in *Proc. Int. Conf. Microw. Millim. Wave Technol. (ICMMT)*, Guangzhou, China, May 2019, pp. 1–3.

[38] M. Pirro *et al.*, "Novel topology for a non-reciprocal MEMS filter," in *Proc. IEEE Int. Ultrason. Symp. (IUS)*, Kobe, Japan, Oct. 2018, pp. 1–3.

[39] M. Pirro, C. Cassella, G. Michetti, and M. Rinaldi, "Low loss non-reciprocal filter for miniaturized RF-Front-End platforms," in *Proc. Joint Conf. IEEE Int. Freq. Control Symp. Eur. Freq. Time Forum (EFTF/IFC)*, Orlando, FL, USA, Apr. 2019, pp. 1–3.

[40] X. Wu, X. Liu, M. D. Hickle, D. Peroulis, J. S. Gómez-Díaz, and A. A. Melcon, "Isolating bandpass filters using time-modulated resonators," *IEEE Trans. Microw. Theory Techn.*, vol. 67, no. 6, pp. 2331–2345, Jun. 2019.

[41] X. Wu, M. Nafe, A. Melcón, J. S. Gómez-Díaz, and X. Liu, "Frequency tunable non-reciprocal bandpass filter using time-modulated microstrip λg/2 resonators," *IEEE Trans. Circuits Syst. II, Exp. Briefs*, vol. 68, no. 2, pp. 667–671, Feb. 2021.

[42] A. Ashley and D. Psychogiou, "Non-reciprocal RF-bandpass filters using transistor-based microwave resonators," in *Proc. 49th Eur. Microw. Conf. (EuMC)*, Paris, France, Oct. 2019, pp. 603–606.

[43] D. M. Pozar, *Microwave Engineering*, 4th Ed. New York, NY, USA: Wiley, 2012.

Andrea Ashley (Graduate Student Member, IEEE) was born in Tulsa, OK, USA in 1992. She received the B.S. degree in mechanical and electrical engineering from Kettering University, Flint, MI, USA, in 2014, and the M.S. degree in electrical engineering from the University of Colorado Boulder, Boulder, CO, USA, in 2019, where she is currently pursuing the Ph.D. degree in electrical engineering.

Her current research interests include the design, characterization, and synthesis of reconfigurable microwave non-reciprocal RF filters and circulators.

Mrs. Ashley is a member of the IEEE Microwave Theory and Techniques Society and the Applied Computational Electromagnetics Society. She was a recipient of the 2018 National Defense Science and Engineering Graduate Fellowship, the ECEE Gold Award for Research, the 2018 EuMC Young Engineer Prize, and the University of Colorado's Dean's Graduate Assistantship.

Dimitra Psychogiou (Senior Member, IEEE) received the Dipl.-Eng. degree in electrical and computer engineering from the University of Patras, Patras, Greece, in 2008, and the Ph.D. degree in electrical engineering from the Swiss Federal Institute of Technology (ETH), Zürich, Switzerland, in 2013.

She is currently a Professor of electrical and electronic engineering at University College Cork (UCC) and Tyndall National Institute, Cork Ireland. Prior to joining UCC, she was a Sr. Research Scientist with Purdue University, West Lafayette, IN, USA, and an Assistant Professor with the University of Colorado Boulder, Boulder, CO, USA. Her research has been presented in more than 160 IEEE publications. Her current research interests include the RF design and characterization of reconfigurable microwave and millimeter-wave passive components, RF-MEMS, acoustic wave resonator-based filters, tunable filter synthesis, and frequency-agile antennas.

Dr. Psychogiou is a Senior Member of URSI and a member of the IEEE MTT-S Filters and Passive Components (MTT-5) and Microwave Control Materials and Devices (MTT-13) Committees. She received the 2020 CAREER Award from the National Science Foundation (NSF), the 2020 URSI Young Scientist Award, and the Junior Faculty Outstanding Research Award from UC Boulder. Furthermore, she serves on the Technical Review Board of various IEEE and EuMA conferences and journals and is the Chair of MMT-13 and the Secretary of the USNC-URSI Commission. She is an Associate Editor of the IEEE MICROWAVE AND WIRELESS COMPONENTS LETTERS and the *International Journal of Microwave and Wireless Technologies*. Previously, she was an Associate Editor of the *IET Microwaves, Antennas and Propagation Journal*.

Authorized licensed use limited to: UNIVERSITY OF COLORADO. Downloaded on December 11,2021 at 20:21:34 UTC from IEEE Xplore. Restrictions apply.